System Identification and Full Flight-Envelope Model Stitching of a Package-Delivery Octocopter

Anthony Gong* and Frank C. Sanders†

San Jose State University Research Foundation, Moffett Field, CA, 94035, USA

Ronald A. Hess‡

University of California - Davis, Davis, CA, 95616, USA

Mark B. Tischler§

U.S. Army Aviation Development Directorate, AMRDEC, Moffett Field, CA, 94035, USA

Multirotors used for package delivery have high thrust-to-weight ratios, but adding heavy payloads to the vehicle can negatively impact the performance of the control system. Accurate models are required to properly design flight controls for the wide range of packages they can carry. Stitched models are continuous, full flight-envelope, quasi-linear parameter varying simulation models that allow for extrapolation to off-nominal conditions. Stitching together flight identified point models with trim data is an attractive approach towards effectively and accurately modeling the entire flight envelope and loading configurations of package delivery multirotors. A custom octocopter platform capable of carrying heavy payloads was built and flight tested. Linear models at 0-, 10-, and 20-knot are identified using frequency domain techniques and verified in the time domain. The point models are stitched together along with trim data to produce a continuous full flight-envelope stitched model that was validated at the anchor points. The stitched model re-trimmed and re-linearized at the heavy configuration shows good agreement with the truth data.

I. Introduction

The simplicity and low-cost nature of multirotor unmanned aerial vehicles (UAV) have resulted in their mass adoption into various industries, in particular, package delivery. Given their high performance (thrust-to-weight ratios greater than 2), multirotors are capable of carrying payloads much greater than their own weight. In such instances, if unaccounted for, the package's mass properties (mass, center of gravity, inertia) can cause degradation and even instability of the closed-loop dynamic system. Accurate models of the vehicle with a payload are needed to properly adjust the flight control system.

Simple rigid body models are sufficient to capture the aerodynamics and performance of multirotors, but aerodynamic modeling of the multiple rotor-to-rotor and rotor-to-body interactions, particularly in forward flight, is more complicated. Bresciani used blade element theory to estimate the drag of the rotor blades of a quadrotor [1]. Bangura and Mahony accounts for various forms of drag including translational, parasitic, induced, and profile in simulation but do not validate their lumped drag parameter with flight tests [2]. Niemiec and Gandhi used a 10-state Peters-He inflow model to calculate the forces and moments at each rotor hub [3].

Model stitching has become a popular way of combining discrete linear point models and trim data together to form a continuous, full flight-envelope simulation model. Zivan and Tischler developed a stitched model of the Bell 206 helicopter [4]. In recent years, stitched models of the Calspan Learjet, F-16 VISTA, and 3DR Iris+ quadrotor have also been developed [5–7]. Stitched models are an attractive method for full flight-envelope modeling of small UAVs since it requires a relatively low number of flight hours to gather the necessary data for identification and stitching. They have also been shown to accurately produce linear point models at off-nominal flight conditions (such as a heavy configuration with a payload [7]), so it makes model stitching an efficient and attractive choice to model a package

---

*Ph.D. Student, Department of Mechanical and Aerospace Engineering, University of California, Davis, AIAA Member

†Senior Research Associate, San Jose State University Research Foundation, AIAA Member

‡Professor Emeritus, Department of Mechanical and Aerospace Engineering, University of California, Davis, AIAA Fellow

§Senior Scientist, U.S. Army Aviation Development Directorate, AMRDEC, Moffett Field, CA, AIAA Associate Fellow

delivery vehicle for rapid flight control design on-demand. Model stitching enables flight control design across the flight envelope with various loading configurations by extrapolation that is inherent to the architecture, thus allowing *deterministic adaptation* of the flight controller to the known payload's mass parameters.

This paper provides a detailed treatment of system identification and model stitching of an octocopter representative of a package-delivery vehicle and validates the model and extrapolation accuracy with flight data. It starts by introducing the flight vehicle in Section II. It is followed by an overview of the system identification methodology in Section III which includes an overview of the flight tests, identified state space models, and verification. Section IV briefly describes modeling stitching, the octocopter stitched model, its flight validation, and extrapolation results. Finally, conclusions are provided in Section V.

II. Flight Vehicle

The flight vehicle is a custom-built octocopter designed to serve as a generic package-delivery vehicle. It operates on two 10,000 mAh lithium polymer batteries, a Pixhawk 2 "Cube" flight controller, and a carbon fiber airframe (Fig. 1). The eight KDE-4213 motors rotate 18-inch carbon fiber blades, producing a maximum of 8 pounds of thrust each. The octocopter has a weight of 18.0 pounds, a motor-to-motor distance of 4.16 feet, thrust-to-weight ratio of 3.55, maximum effective payload of 40 pounds, and a hovering flight time of 20 minutes. The large airframe and high performance provides flexibility for hardware modifications allowing package-delivery research.

A large cargo bay (24.0 in x 24.0 in x 11.0 in) is designed with a carbon fiber internal structure for rigidity and encased in foam to form the exterior. The cargo bay also houses servos which actuate an opening mechanism that allows for it to drop off the payload, although it was not used during flight tests. The cargo bay allows for a wide range of *internal* payloads while keeping the drag characteristics of the aircraft constant throughout flight tests with varying loading configurations.

**Fig. 1   Octocopter platform equipped with a large cargo bay.**

A. Software

The Pixkawk 2 flight computer runs a custom, modified version of Arducopter v3.5.3 using the "pictures-to-code" process described in [8] and shown in Fig. 2. In short, MATLAB Embedded Coder® is used to auto-code a set of library files to drive a custom Arducopter flight mode that enables automated frequency sweep injection, feedback controller

design, and data collection. This methodology allows a block diagram designed in Simulink® to be rapidly deployed onto the flight computer with minimal coding in C++.
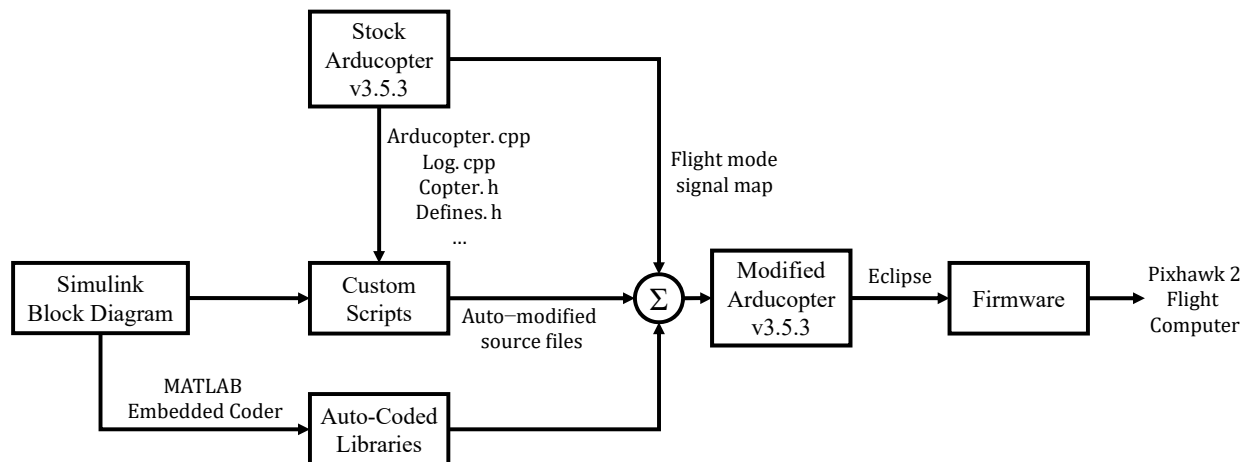
**Fig. 2 Schematic of the "pictures-to-code" process.**

B. Loading Configurations

The aircraft is tested under two, nominal and heavy, configurations. The nominal configuration is defined as the octocopter carrying an *empty, unloaded* cargo bay whereas the heavy configuration carries 11.7 pounds (31.9% of the heavy configuration's takeoff weight) specifically loaded into a corner. The payload consists of a metal container housing two additional flight batteries fixed in placed by stiff foam blocks to prevent movement in flight (Fig. 3). The heavy container is rigidly mounted to the bottom of the forward-right corner of the cargo bay to shift the center of gravity as far away from the center as possible. This corner-loaded heavy configuration is designed to represent an off-nominal scenario to validate the stitched model's extrapolation capabilities described in Section IV. The two flight batteries within the cargo bay are connected to extend the flight time and expedite the data collection process while in the heavy configuration.

Table 1 summarizes the mass properties of the two configurations. The nominal (empty cargo bay) configuration has a center of gravity directly below the flight computer (i.e. only a z-axis center of gravity shift downwards), and the 11.7 lb. payload of the heavy configuration shifts the z-axis center of gravity further down while also shifting the x- and y-axis centers of gravity due to being specifically loaded in the corner. Body axes are used where the x-axis points (positive) forward, y-axis points (positive) towards the right, and z-axis (positive) down. The center of gravity locations are measured from the sensors on-board the Pixhawk 2 (above the cargo bay) and the moments of inertia are in directions parallel to the body axes and calculated at the each configuration's respective center of gravity.

Table 1 Mass properties of the vehicle's nominal and heavy configurations.

Parameter	Nominal (Unloaded)	Heavy
Weight [lb]	25.0	36.7
x_{cg} [ft]	0	0.167
y_{cg} [ft]	0	0.188
z_{cg} [ft]	0.310	0.458
I_{xx} [slug-ft^2]	0.656	0.885
I_{yy} [slug-ft^2]	0.730	0.911
I_{zz} [slug-ft^2]	1.098	1.205
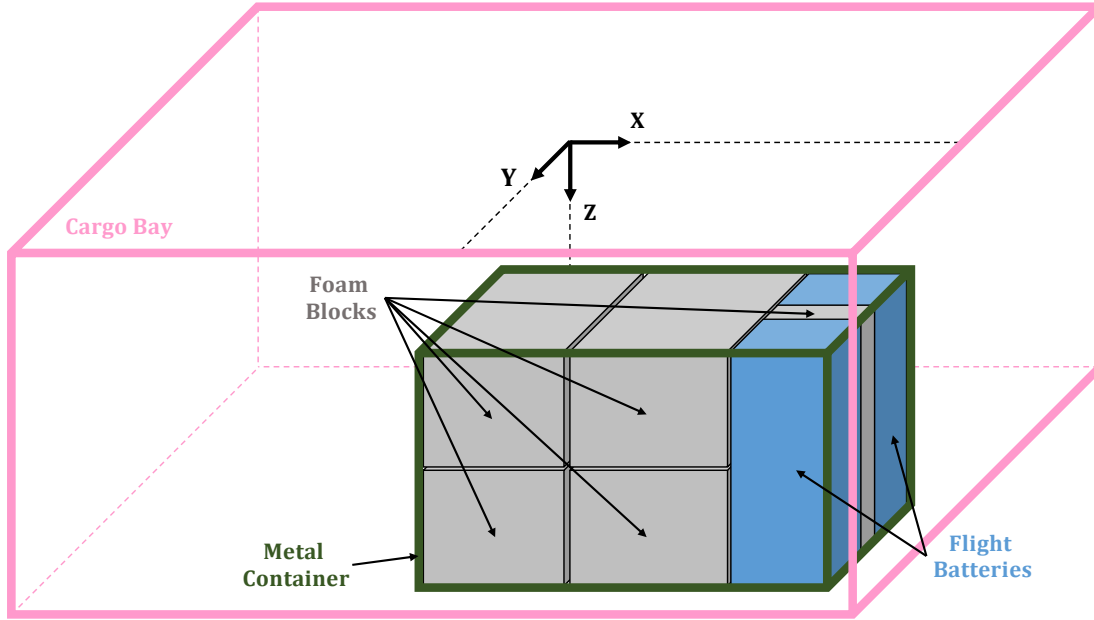
Fig. 3 Diagram of the corner-loaded payload of the the heavy configuration.

III. System Identification

A comprehensive frequency response method of system identification [9] developed by the Aviation Development Directorate (ADD) and Universities Space Research Associates (USRA) is encompassed by the CIFER® software package. Figure 4 shows an overview of the frequency domain identification methodology. Broadly speaking, it involves flight testing to collect frequency sweep data, generating conditioned frequency responses, identifying a state space model from them, and verifying the model with dissimilar data.

This methodology is used to identify three state-space models of the *nominal* configuration at $U_0 = 0$, 10, and 20 knots to serve as anchor points for model stitching. Identification is intentionally performed on the nominal (empty) configuration since the cargo bay's contribution to the dynamics will be included in the models.

A. Flight Tests

Flight tests were conducted outdoors during early mornings in windless conditions. The pilot engages the custom flight mode and uses a combination of switches and knobs on the radio transmitter to control the engagement and magnitude of automated sweeps and doublets (Fig. 5). The frequency sweeps spanned 0.628-62.8 rad/sec (0.1-10 Hz) over the course of 30 seconds with 2 seconds of trim before and after. A 10-second fade-in was used to keep the aircraft response near trim during the low frequency portion of the sweeps. Sweep magnitudes were adjusted for each axis to target a desired response as shown in Table 2. Doublets occurred over a 5-second period with 1-second pulses in both the positive and negative directions with the same magnitude as the corresponding frequency sweep of that axis. Figure 6 shows a series of time responses for a longitudinal sweep and doublet in hover. Two sweeps and doublets were collected per axis per flight condition.

Table 2 Targeted peak magnitudes during frequency responses.

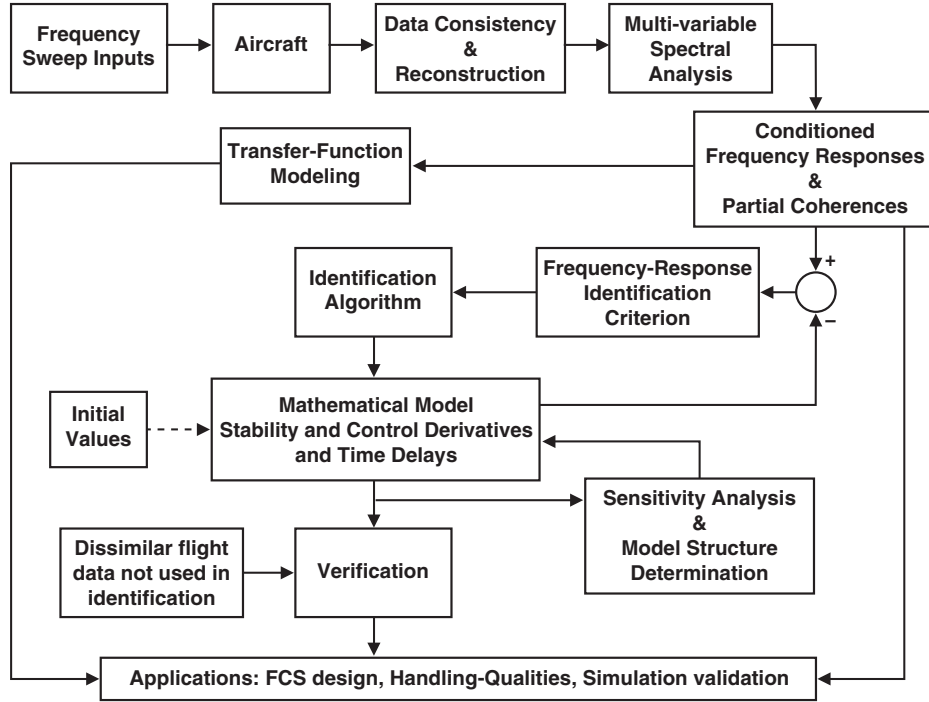| Axis	Desired Rate Response	Maximum Desired Response
Roll/Pitch	$p, q = \pm 100 \frac{\text{deg}}{\text{sec}}$	$\phi, \theta = \pm 15$ deg
Heave	$w = \pm 5 \frac{\text{feet}}{\text{sec}}$	$P_D = \pm 25$ feet
Yaw	$r = \pm 40 \frac{\text{deg}}{\text{sec}}$	$\psi = \pm 45$ deg

Fig. 4 Overview of the frequency domain system identification methodology [9].

All flight tests were conducted in a modified version of the "Stabilize" flight mode in Arducopter that allowed for custom injection of automated signals and data logging of all relevant signals at 100 Hz. The flight mode is a robustly stable inner-loop control system that does not rely on GPS measurements for stability and is adequate for conducting frequency sweeps with both the nominal and heavy configurations. Individual motor commands were monitored to ensure that motor saturation did not occur in flight. The automated signal, δ_{auto}, is summed with the pilot commands and the four resulting mixer inputs ($\delta_{lat}, \delta_{lon}, \delta_{thr}, \delta_{yaw}$) are used for the identification of the *bare-airframe* (mixer, actuator, and octocopter) as seen in Fig. 5. It can be seen from visual inspection that the mixer input signal is relatively clean despite the automated sweep being injected at the pilot command during a *closed-loop* flight test (Fig. 6a). The aircraft's position, velocity, angular velocity, attitude (all provided by the extended Kalman filter), and all three redundant accelerometer signals are logged for identification.
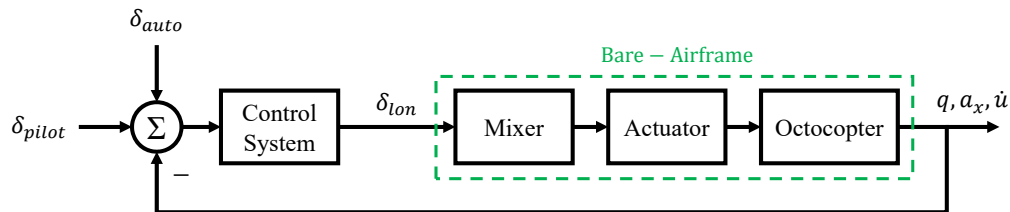
Fig. 5 General schematic showing automated signal injection point and the identified bare-airframe (pitch axis shown).

Trim shot data were collected from hover out to roughly 25 knots. Longitudinal trim was added to the pilot command at -5% increments to command an increasing (negative) pitch attitude. The aircraft was allowed to cruise for 10 seconds in steady-state before proceeding to the next trim value. An on-board variometer provided audio feedback that allowed the pilot to locate and provide the necessary throttle input required to trim the aircraft for steady, level flight.

Flight tests for both (nominal and heavy) configurations were conducted in the same manner.
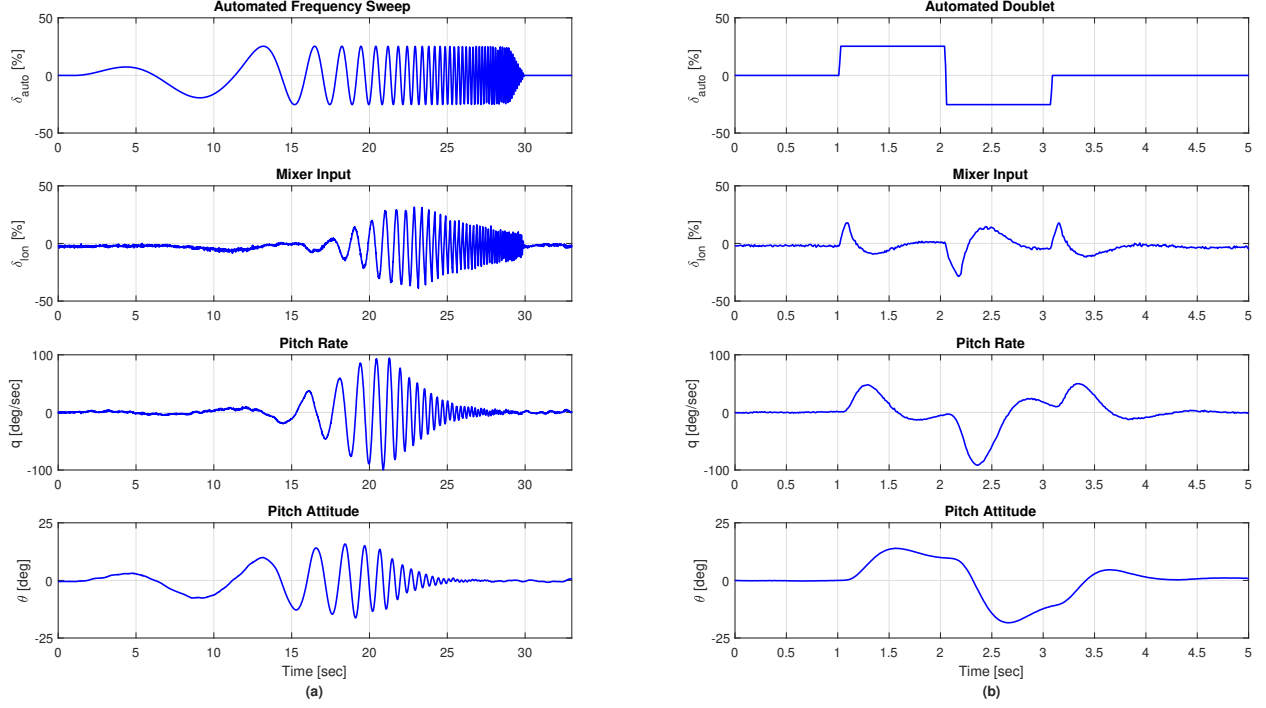
Fig. 6 Example longitudinal axis flight data from automated a.) frequency sweeps and b.) doublets in hover.

B. State-Space Model Identification

The state-space structure of the bare-airframe is a 6-DOF (degree-of-freedom) rigid body model with time delays (τ) (Eq. 1) and first-order actuators.

$$\mathbf{M}\dot{\mathbf{x}} = \mathbf{F}\mathbf{x} + \mathbf{G}\mathbf{u}(t - \tau)$$
$$\mathbf{y} = \mathbf{H_0}\mathbf{x} + \mathbf{H_1}\dot{\mathbf{x}}$$
(1)

$$\mathbf{x} = [u \ \ v \ \ w \ \ p \ \ q \ \ r \ \ \phi \ \ \theta \ \ \psi \ \ \delta'_{lat} \ \ \delta'_{lon} \ \ \delta'_{thr} \ \ \delta'_{yaw}]^{\mathrm{T}}$$
$$\mathbf{y} = [\dot{u} \ \ \dot{v} \ \ \dot{w} \ \ p \ \ q \ \ r \ \ a_x \ \ a_y \ \ a_z]$$

As seen from Table 1, both the nominal and heavy configurations have center of gravity locations *below* the sensors located within the flight computer. The offsets (x_a, y_a, z_a) from Eq. 2 are incorporated into the output matrix ($\mathbf{H_1}$) of Eq. 1 to correct the model to the sensors during the system identification process. The accelerometer signals (a_x, a_y, a_z) and body-axis accelerations ($\dot{u}$, $\dot{v}$, $\dot{w}$) are corrected for offsets in the $\mathbf{H_1}$ matrix since they are reconstructed from accelerometer data measured at the sensors [9].

The resulting augmented state-space structure used in identification is shown in Eq. (3).

$$a_x = \dot{u} + W_0 q - V_0 r + (g \ \cos\Theta_0)\theta + z_a\dot{q} - y_a\dot{r}$$
$$a_y = \dot{v} + U_0 r - W_0 p - (g \ \cos\Theta_0)\phi - z_a\dot{p} + x_a\dot{r}$$
$$a_z = \dot{w} + V_0 p - U_0 q + (g \ \sin\Theta_0)\theta + y_a\dot{p} - x_a\dot{q}$$
(2)

$$
\begin{bmatrix}
1 & 0 & 0 & 0 & 0 & 0 & 0 & 0 & 0 & 0 & 0 & 0 & 0 \\
0 & 1 & 0 & 0 & 0 & 0 & 0 & 0 & 0 & 0 & 0 & 0 & 0 \\
0 & 0 & 1 & 0 & 0 & 0 & 0 & 0 & 0 & 0 & 0 & 0 & 0 \\
0 & 0 & 0 & 1 & 0 & 0 & 0 & 0 & 0 & 0 & 0 & 0 & 0 \\
0 & 0 & 0 & 0 & 1 & 0 & 0 & 0 & 0 & 0 & 0 & 0 & 0 \\
0 & 0 & 0 & 0 & 0 & 1 & 0 & 0 & 0 & 0 & 0 & 0 & 0 & \tau_{lead} \\
0 & 0 & 0 & 0 & 0 & 0 & 1 & 0 & 0 & 0 & 0 & 0 & 0 \\
0 & 0 & 0 & 0 & 0 & 0 & 0 & 1 & 0 & 0 & 0 & 0 & 0 \\
0 & 0 & 0 & 0 & 0 & 0 & 0 & 0 & 1 & 0 & 0 & 0 & 0 \\
0 & 0 & 0 & 0 & 0 & 0 & 0 & 0 & 0 & 1 & 0 & 0 & 0 \\
0 & 0 & 0 & 0 & 0 & 0 & 0 & 0 & 0 & 0 & 1 & 0 & 0 \\
0 & 0 & 0 & 0 & 0 & 0 & 0 & 0 & 0 & 0 & 0 & 1 & 0 \\
0 & 0 & 0 & 0 & 0 & 0 & 0 & 0 & 0 & 0 & 0 & 0 & 1
\end{bmatrix}
\begin{bmatrix}
\dot{u} \\ \dot{v} \\ \dot{w} \\ \dot{p} \\ \dot{q} \\ \dot{r} \\ \dot{\phi} \\ \dot{\theta} \\ \dot{\psi} \\ \dot{\delta}'_{lat} \\ \dot{\delta}'_{lon} \\ \dot{\delta}'_{thr} \\ \dot{\delta}'_{yaw}
\end{bmatrix}
=
$$

$$
\begin{bmatrix}
X_u & X_v & X_w & X_p & X_q-W_0 & X_r+V_0 & 0 & -g\cos(\Theta_0) & 0 & X_{lat} & X_{lon} & X_{thr} & X_{yaw} \\
Y_u & Y_v & Y_w & Y_p+W_0 & Y_q & Y_r-U_0 & g\cos(\Theta_0) & 0 & 0 & Y_{lat} & Y_{lon} & Y_{thr} & Y_{yaw} \\
Z_u & Z_v & Z_w & Z_p-V_0 & Z_q+U_0 & Z_r & 0 & -g\sin(\Theta_0) & 0 & Z_{lat} & Z_{lon} & Z_{thr} & Z_{yaw} \\
L_u & L_v & L_w & L_p & L_q & L_r & 0 & 0 & 0 & L_{lat} & L_{lon} & L_{thr} & L_{yaw} \\
M_u & M_v & M_w & M_p & M_q & M_r & 0 & 0 & 0 & M_{lat} & M_{lon} & M_{thr} & M_{yaw} \\
N_u & N_v & N_w & N_p & N_q & N_r & 0 & 0 & 0 & N_{lat} & N_{lon} & N_{thr} & N_{yaw} \\
0 & 0 & 0 & 1 & 0 & \tan(\Theta_0) & 0 & 0 & 0 & 0 & 0 & 0 & 0 \\
0 & 0 & 0 & 0 & 1 & 0 & 0 & 0 & 0 & 0 & 0 & 0 & 0 \\
0 & 0 & 0 & 0 & 0 & \sec(\Theta_0) & 0 & 0 & 0 & 0 & 0 & 0 & 0 \\
0 & 0 & 0 & 0 & 0 & 0 & 0 & 0 & -\omega_{lag} & 0 & 0 & 0 & 0 \\
0 & 0 & 0 & 0 & 0 & 0 & 0 & 0 & 0 & -\omega_{lag} & 0 & 0 & 0 \\
0 & 0 & 0 & 0 & 0 & 0 & 0 & 0 & 0 & 0 & -\omega_{lag} & 0 & 0 \\
0 & 0 & 0 & 0 & 0 & 0 & 0 & 0 & 0 & 0 & 0 & -\omega_{lag} & 0
\end{bmatrix}
\begin{bmatrix}
u \\ v \\ w \\ p \\ q \\ r \\ \phi \\ \theta \\ \psi \\ \delta'_{lat} \\ \delta'_{lon} \\ \delta'_{thr} \\ \delta'_{yaw}
\end{bmatrix}
+
$$

$$
\begin{bmatrix}
0 & 0 & 0 & 0 \\
0 & 0 & 0 & 0 \\
0 & 0 & 0 & 0 \\
0 & 0 & 0 & 0 \\
0 & 0 & 0 & 0 \\
0 & 0 & 0 & 0 \\
0 & 0 & 0 & 0 \\
0 & 0 & 0 & 0 \\
0 & 0 & 0 & 0 \\
\omega_{lag} & 0 & 0 & 0 \\
0 & \omega_{lag} & 0 & 0 \\
0 & 0 & \omega_{lag} & 0 \\
0 & 0 & 0 & \omega_{lag}
\end{bmatrix}
\begin{bmatrix}
\delta_{lat} \\ \delta_{lon} \\ \delta_{thr} \\ \delta_{yaw}
\end{bmatrix}
\left(t -
\begin{bmatrix}
\tau_{lat} \\ \tau_{lon} \\ \tau_{thr} \\ \tau_{yaw}
\end{bmatrix}
\right)
\tag{3}
$$

1. Actuator Models

The bare-airframe is identified from the mixer input, so that the actuators downstream of the mixer are lumped into the identification. The sweeps used for identification span a large frequency range and consequently captures the actuator's effective bandwidth. Therefore, actuator models must be included to capture the frequency response data out to maximum usable frequencies. Figure 7a shows that the pitch rate response has a clear -40 dB/decade roll-off at high frequency that is not captured in the 6-DOF hover pitch rate model which has a 2nd-over-3rd order form characterized by the hovering cubic denominator and naturally rolls off at -20 dB/dec (Eq. 4) [9].

$$
\frac{q}{\delta_{lon}}(s) = \frac{M_{\delta_{lon}} s (s - X_u)}{(s + 1/T_{hc})[\zeta_{hc}, \omega_{hc}]}
\tag{4}
$$

The actuators are modeled as first-order transfer functions, so four additional states (one for each axis) are added to the the typical 9 rigid body states. The actuator "lags" were identified as a free parameter and constrained to be equal on all four axes since the octocopter operates eight identical actuators. Equation (5) shows an example of how the lagged input (δ') is related to the commanded input (δ).

$$
\frac{\delta'}{\delta}(s) = \frac{\omega_{lag}}{s + \omega_{lag}}
$$
$$
\dot{\delta}' = \omega_{lag}(\delta - \delta')
\tag{5}
$$

Additionally, a single actuator (motor, propeller, and electronic speed controller combination) was mounted to a thrust stand capable of measuring forces, torques, angular velocities, and vibrations in all three axes and swept up to 100 rad/sec. Fig. 7b shows that the excellent fit ($J = 20.1$) of a first-order transfer function (Eq. 6) to the actuator's force response ($\frac{F}{\delta_{pwm}}$) from thrust stand data confirms that the additional roll-off seen in Fig. 7a is in fact the actuator dynamics. The lag identified by the thrust stand fit ($\omega_{lag} = 18.88$ rad/sec), agrees very well with the values identified from the 0-knot model, so the parameter was fixed during the identification of the 10- and 20-knot models.

$$\frac{F}{\delta_{pwm}} = \frac{0.247}{s + 18.88}e^{-0.055s} \tag{6}$$

Fig. 7 A first-order actuator model captures the (a) additional -20 dB/dec rolloff in the pitch rate response above 10 rad/sec, and a (b) first-order transfer function fit of the actuator's force response from thrust stand data.

The octocopter generates yaw rate from differential motor torques unlike the other axes which use collective or differential forces. The difference can be seen in Fig. 8a, where the phase of the yaw rate response is fairly constant between 1.0-10 rad/sec indicating some lead between the input and output. An additional free parameter, τ_{lead}, seen in the **M** matrix of Eq. (3) is identified to capture the constant-phase effect. The yaw rate equation then becomes,

$$\dot{r} + \tau_{lead}\,\dot{\delta}'_{yaw} = N_r r + N_{yaw}\delta'_{yaw} \tag{7}$$

Solving for the $\frac{r}{\delta_{yaw}}(s)$ response yields Eq. (8) which shows that the τ_{lead} parameter determines the location of an extra zero that allows the identification algorithm to capture the effect.

$$\frac{r}{\delta_{yaw}} = \left(\frac{1}{s - N_r}\right)\left(\frac{\omega_{lag}}{s + \omega_{lag}}\right)(N_{yaw} - \tau_{lead}\,s) \tag{8}$$

Fig. 8b shows that the additional zero helps to capture the correct yaw rate response to a doublet.

2. Model Structure Reduction

The model structure is reduced by analyzing the magnitude, phase, and coherence of each frequency response. Responses that do not have frequency ranges of coherence that meet the cutoff and range requirements (Eq. 9) are set to
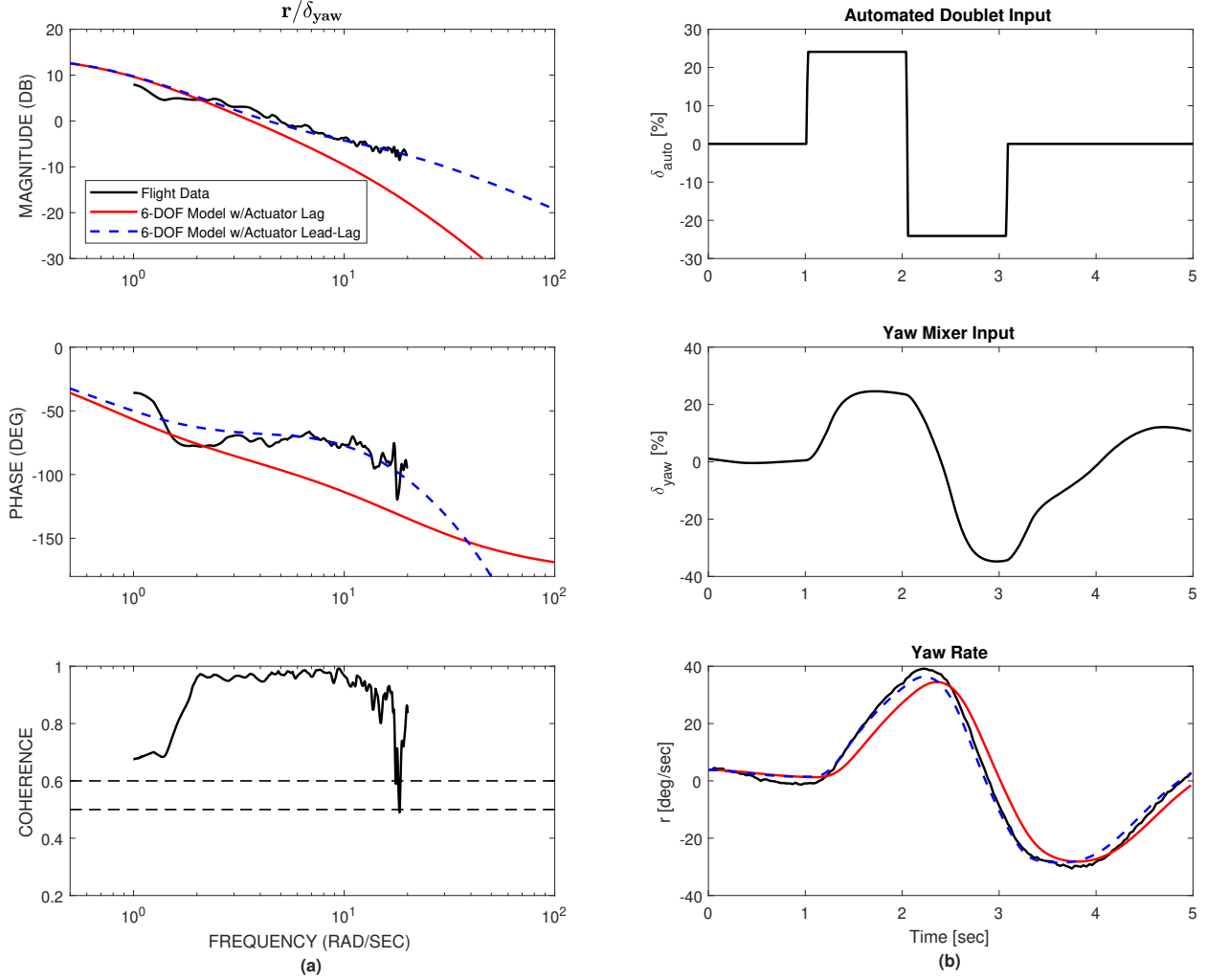
Fig. 8 Comparison of a yaw axis (a) frequency response and (b) time response to a doublet with various actuator models at 0-knots.

zero and some derivatives (identification parameters) are fixed to zero based on the equations of motion as explained in [9].

$$(\hat{\gamma}_{xy}^2)_{(\omega_{min}, \omega_{max})} \geq 0.50$$
$$\log(\frac{\omega_{max}}{\omega_{min}}) \geq 0.30 \tag{9}$$

For example, the pitch acceleration equation is given in Eq. (10).

$$\dot{q} = M_u u + M_v v + M_w w + M_p p + M_q q + M_r r + M_{\delta_{lat}} \delta_{lat} + M_{\delta_{lon}} \delta_{lon} + M_{\delta_{thr}} \delta_{thr} + M_{\delta_{yaw}} \delta_{yaw} \tag{10}$$

Taking the LaPlace transform, the off-axis response, pitch rate to lateral input, is then

$$\frac{q}{\delta_{lat}}(s) = (\frac{1}{s - M_q})[M_{\delta_{lat}} + M_u \frac{u}{\delta_{lat}}(s) + M_v \frac{v}{\delta_{lat}}(s) + M_w \frac{w}{\delta_{lat}}(s) + M_p \frac{p}{\delta_{lat}}(s) + M_r \frac{r}{\delta_{lat}}(s)] \tag{11}$$

As seen in Fig. 9, this particular off-axis response does not meet the coherence requirement, so it is set to zero ($\frac{q}{\delta_{lat}}(s) = 0$). Since the on-axis responses $\frac{p}{\delta_{lat}}(s)$ and $\frac{v}{\delta_{lat}}(s)$ both have good coherence and are non-zero, the derivatives $M_{\delta_{lat}}$, M_v, and M_p must be zero for Eq. (11) to be zero and are subsequently fixed during the identification process.[9]

9
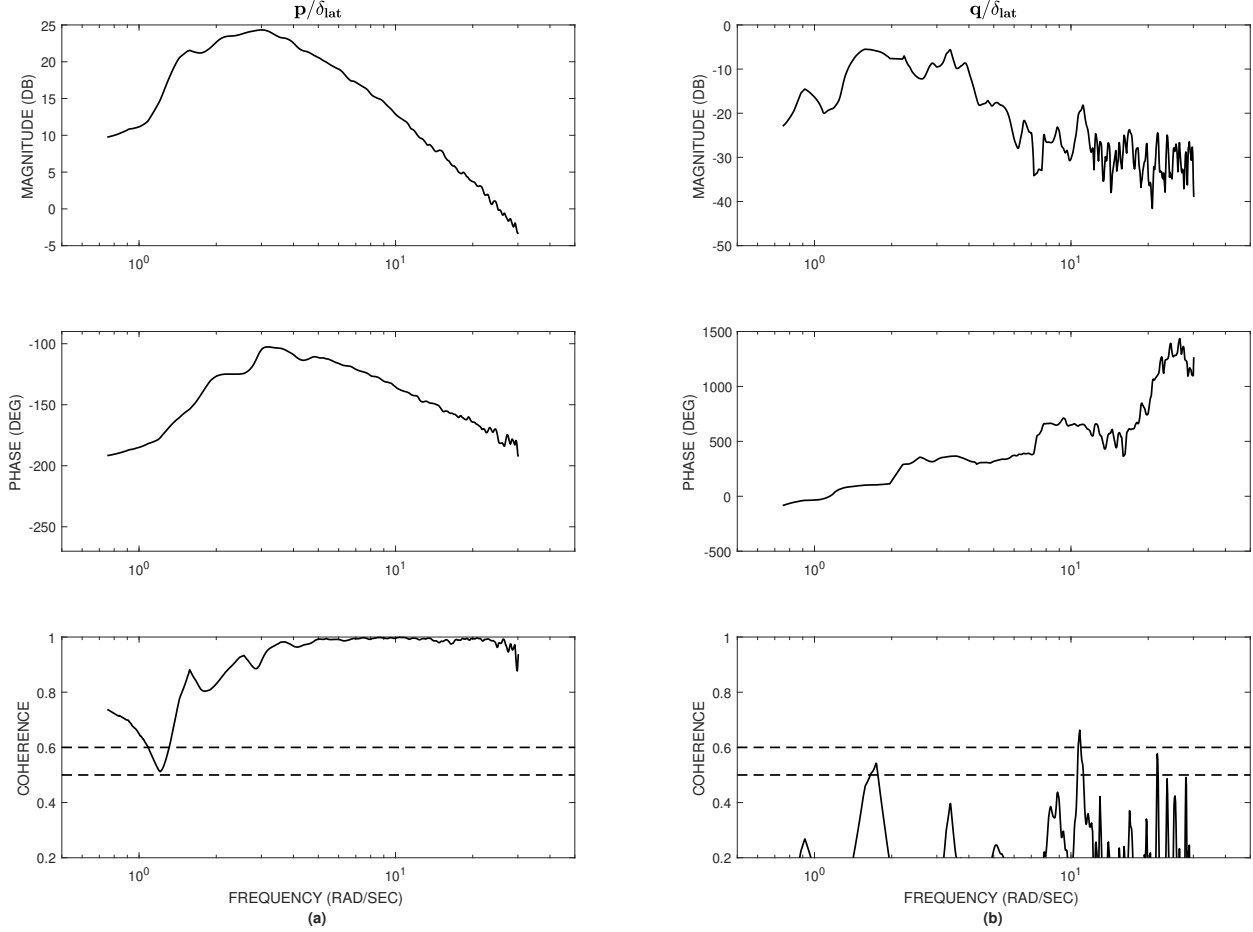
Fig. 9 Example flight responses in hover of an a.) on-axis response with good coherence and b.) off-axis response with poor coherence analyzed during the model reduction process.

The model structure is further reduced by iteratively fixing parameters with high insensitivities (I > 10%) and Cramer-Rao percentages (CR% > 20%) to zero [9]. Parameters with high insensitivities do not have an impact on the responses used in the identification and those with high Cramer-Rao bounds are not known with acceptable certainty.

Table 3 shows the identification results for the 0-, 10-, and 20-knot models. It shows that the rate damping derivatives, M_q and L_p, are absent from the hover model. Previous works have also shown that multirotors have very little rate damping in hover [7, 8]. However, in forward flight, those derivatives become dominant and the speed derivatives, M_u and L_v, which dominated the hover response, become either very small or are dropped during iterative model reduction. The stock octocopter has near-perfect symmetry, but the added cargo bay and its internal structure changes the aircraft's moments of inertia enough to produce a small difference in the control derivatives, $L_{\delta_{lat}}$ and $M_{\delta_{lon}}$. Figure 10 shows that the identified hover model agrees very well with the frequency responses obtained from flight data.

Table 4 shows that the average cost of the 0-, 10-, and 20-knot models were 75.23, 90.66, and 61.88, respectively. The cost is computed based on weighted sum of square errors in the magnitude and phase of each frequency response [9] seen in Eq. (12). $J_{ave} < 100$ is considered acceptable while $J_{ave} < 50$ is considered a perfect model [9].

$$J = \sum_{l=1}^{n_{TF}} \left\{ \frac{20}{n_\omega} \sum_{\omega_1}^{\omega_{n_\omega}} W_\gamma [W_g(|\hat{T}_c| - |T|)^2 + W_p(\angle T_c - \angle T)^2] \right\}_l \tag{12}$$

10
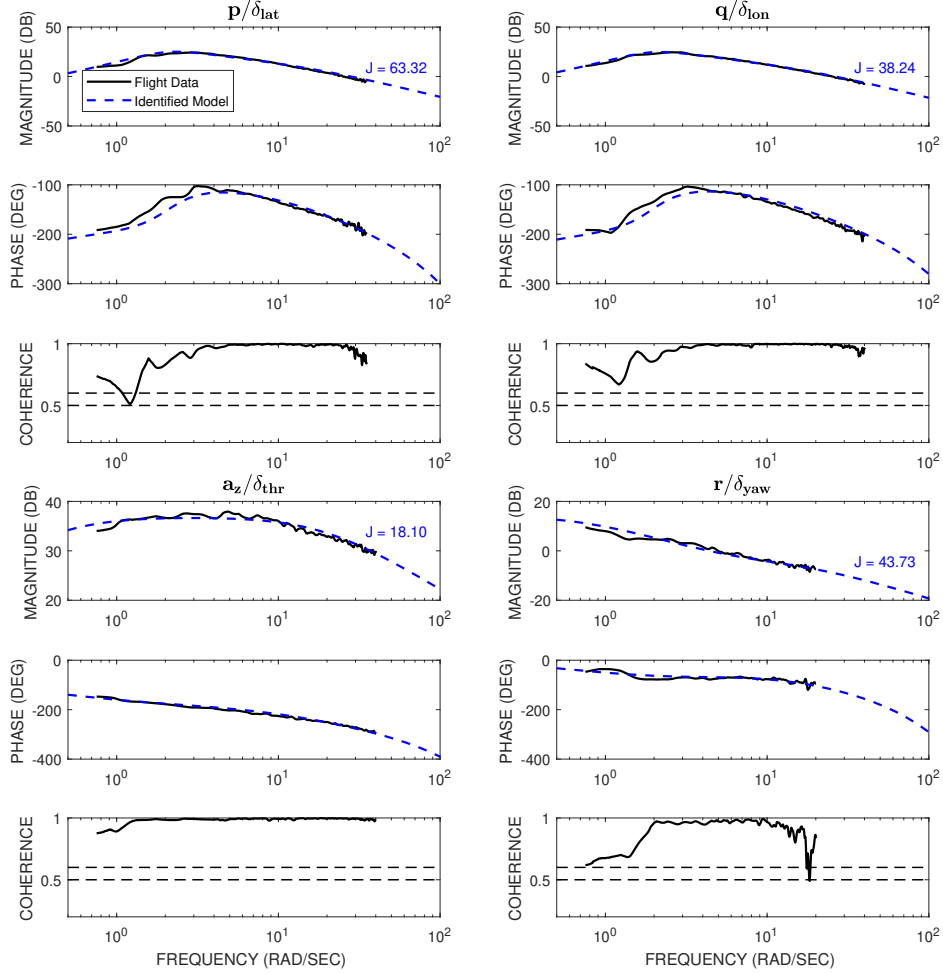
Fig. 10 On-axis responses of the identified 0-knot model compared with flight data.

C. Model Verification

The models are verified using dissimilar flight data that were *not* used in the identification process. The identification process is driven by frequency sweep data while the verification is done with the use of doublet responses, shown in Fig. 6b. This ensures that models are not overly tuned to any specific set of data, but are valid over a broad frequency range. The three identified bare-airframe models are all unstable, so integration of equations of motion to any input will cause the time responses to diverge towards infinity at the exponential rate of the unstable poles. Time domain verification is done by driving the bare-airframe models *open-loop* with the *closed-loop* mixer inputs from flight data, corrected for biases and reference shifts. The time domain responses of the 0-knot and 20-knot models show excellent agreement with flight test data in Fig. 11. While the shapes of the airspeed, pitch rate, and x-axis accelerometer look quite similar between the two models, the z-axis accelerometer notably shows no response to the longitudinal doublet near hover, but a definite doublet-like response at 20 knots.

IV. Stitched Model

The linear state space equations described in Eq. (13) are *perturbation* equations. They describe the dynamic response about some *reference* or *trim* condition, U_0, when the aircraft is in steady-state. The aerodynamic trim forces (derived from the collected trim data) and aerodynamic perturbation forces and moments (derived from the identified models) are summed with the nonlinear gravity forces to produce the *total* forces and moments.

Table 3 Final identification parameters for the nominal 0-, 10-, and 20-knot models.

Parameter	0 knots			10 knots			20 knots		
	Value	CR%	I%	Value	CR%	I%	Value	CR%	I%
X_u	-0.28	7.58	3.15	-0.36	11.79	5.81	-0.25	7.87	3.11
Y_v	-0.26	7.84	3.24	-0.29	8.46	3.25	-0.41	21.48	9.11
Z_w	-0.46	22.33	10.69	-0.76	16.57	6.86	-0.73	18.14	8.43
L_v	-0.30	5.89	2.32	-0.11	8.90	3.32	—	—	—
L_p	—	—	—	—	—	—	-1.34	13.23	5.58
M_u	0.25	5.69	2.25	-0.28	11.73	5.26	-0.09	18.95	6.97
M_w	—	—	—	0.37	12.38	4.27	—	—	—
M_q	—	—	—	—	—	—	-0.70	25.26	8.24
N_r	-0.73	24.55	8.68	-1.31	12.94	3.39	1.25	15.94	4.42
$L_{\delta_{lat}}$	50.37	2.89	1.11	45.02	2.30	1.11	51.77	2.51	1.13
$M_{\delta_{lon}}$	45.40	3.04	1.09	47.36	2.62	1.00	45.04	2.03	0.96
$Z_{\delta_{thr}}$	-69.56	4.06	1.85	-67.21	3.78	1.88	-64.87	4.04	1.96
$N_{\delta_{yaw}}$	3.76	7.76	2.61	3.35	7.30	1.65	2.34	9.05	2.94
τ_{lat}	0.02	11.17	4.68	0.02	8.01	4.00	0.03	7.63	3.35
τ_{lon}	0.02	8.97	3.86	0.02	6.71	3.35	0.03	7.04	3.11
τ_{thr}	0.02	10.94	5.17	0.02	10.52	5.22	0.02	13.20	6.50
τ_{yaw}	0.04	19.40	7.54	—	—	—	0.04	37.45	10.61
τ_{lead}	-0.59	8.69	3.23	-0.38	19.48	4.06	-1.09	5.99	1.87
ω_{lag}[1]	18.91	5.33	1.56	18.91	—	—	18.91	—	—

[1] Fixed at the 0-knot value for the 10- and 20-knot models

$$\dot{\mathbf{x}} = \mathbf{A}|_{U_0}\mathbf{x} + \mathbf{B}|_{U_0}\mathbf{u}$$
$$\mathbf{y} = \mathbf{C}|_{U_0}\mathbf{x} + \mathbf{D}|_{U_0}\mathbf{u} \tag{13}$$

For example, the total X-body axis force is:

$$\mathbf{X} = \mathbf{X}_{grav} + \mathbf{X}_{aero}$$
$$= \mathbf{X}_{grav} + (\mathbf{X}_{aero_0} + \Delta\mathbf{X}_{aero}) \tag{14}$$

where the gravity force is:

$$\mathbf{X}_{grav} = m(\bar{\mathbf{X}}_{grav})$$
$$= -m(g \sin \Theta) \tag{15}$$

the dimensional aerodynamic trim force is:

$$\mathbf{X}_{aero_0} = m(\bar{\mathbf{X}}_{aero_0})$$
$$= m(g \sin \Theta_0|_U) \tag{16}$$

and the dimensional aerodynamic perturbation force is:

$$\Delta\mathbf{X}_{aero} = m[(\mathbf{A}_{aero}|_{U_f})\Delta\mathbf{x} + (\mathbf{B}_{aero}|_{U_f})\Delta\mathbf{u}]$$
$$= m[(X_u|_{U_f}\Delta u) + (X_v|_{U_f}\Delta v) + (X_w|_{U_f}\Delta w)$$
$$+ (X_p|_{U_f}\Delta p) + (X_q|_{U_f}\Delta q) + (X_r|_{U_f}\Delta r)$$
$$+ (X_{lat}|_{U_f}\Delta\delta_{lat}) + (X_{lon}|_{U_f}\Delta\delta_{lon}) + (X_{thr}|_{U_f}\Delta\delta_{thr}) + (X_{yaw}|_{U_f}\Delta\delta_{yaw})] \tag{17}$$

Table 4   Individual and average cost for the nominal 0-, 10-, and 20-knot models.

Response	0 knots	10 knots	20 knots
$\dot{v}/\delta_{lat}$	200.89	67.05	27.39
p/δ_{lat}	63.23	21.02	31.57
a_y/δ_{lat}	47.44	205.49	79.90
$\dot{u}/\delta_{lon}$	144.07	44.37	54.91
$\dot{w}/\delta_{lon}$	—	50.04	25.91
q/δ_{lon}	38.24	44.26	28.48
a_x/δ_{lon}	44.07	110.59	179.19
a_z/δ_{thr}	18.10	19.74	64.63
$\dot{v}/\delta_{yaw}$	—	216.10	65.78
r/δ_{yaw}	43.73	127.98	61.04
J_{ave}	75.23	90.66	61.88

For a multirotor which has decoupled dynamics and does not produce any X-body force from its actuators, Eq. (14) then becomes:

$$\mathbf{X} = m[(g \sin \Theta_0|_U) + X_u|_{U_f}(U - U_0) + X_w|_{U_f}(W - W_0) + X_q|_{U_f}Q] \qquad (18)$$

As described in Refs. [9, 10], model stitching involves the combination of linear points models and trim data to produce a quasi-nonlinear simulation model. Discrete linear point models serve as *anchor points* within the architecture and can come from physics-based models or system identification. The dimensional stability and control derivatives are linearly interpolated between the anchor point models and looked up based on the *filtered airspeed*. The stitched model looks-up the necessary derivatives to compute the aerodynamic perturbation forces and utilizes finely spaced trim data to compute the aerodynamic trim forces. This allows the stitched model to continuously simulate the dynamics at non-anchor point conditions. Figure 12 shows a schematic of the model stitching architecture.

A. Octocopter Stitched Model

The stitched model of this package-delivery vehicle is made from the three identified point models and trim shot data collected from flight Fig. 13a. The trim shot data from flight are collected at discrete points, so a rectangular grid at finer, 1-knot, increments is used to produce evenly spaced trim shot data for stitching (Fig. 13b). It is important to note that construction of the stitched model is solely based on data from the *nominal* configuration.

An important objective for this research is to determine the amount data required to construct a stitched model with good predictive accuracy over the entire flight envelope. The goal is to determine the minimum amount of trim shot data and anchor point models required such that the stitched model properly captures the true dynamics and provide a recommendation for accurate and efficient model stitching for multirotors of this size.

B. Model Validation

A validation of the stitched model is conducted by linearizing it at the anchor point trim conditions. Figure 14 shows a comparison between the linearized stitched model and the anchor point model for the 0-knot model. It shows perfect agreement except on the longitudinal axis since the model stitches in the U-body direction. As described in [10], "U-derivatives" (X_u, Z_u, M_u) are *implicitly* represented in the stitched model architecture when "stitching in U" (i.e., $U \equiv U_0$ in Eq. (18)), so there are small differences when compared to the *explicitly* identified U-derivative values. Therefore, $\frac{q}{\delta_{lon}}$ from linearization of the stitched model is expected to differ from the anchor point model at the low-to-mid frequency range due to the differences in X_u and M_u.
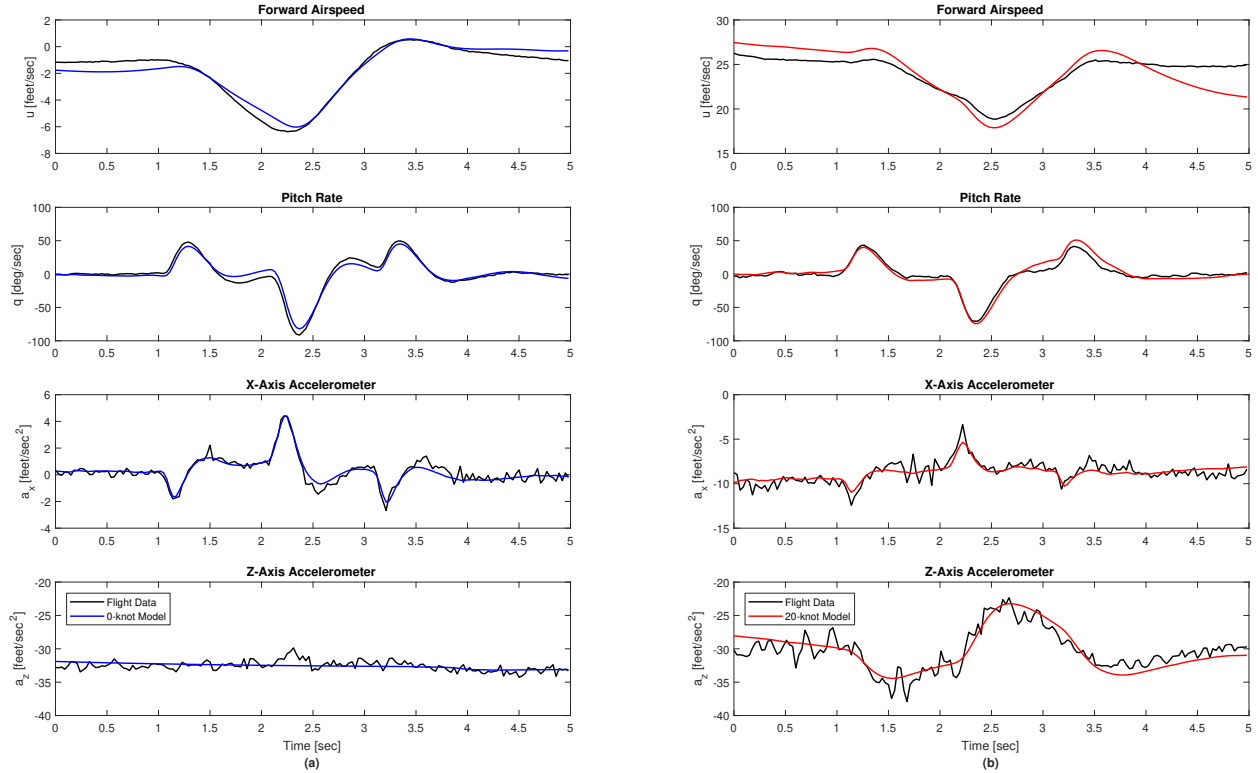
Fig. 11   Time domain verification of the identified (a). 0-knot and (b). 20-knot models with flight data of a doublet input on the longitudinal axis.

C. Model Extrapolation

The stitched model is capable of extrapolating to off-nominal conditions such as the heavy (mass, center of gravity, inertia) configuration even though it is constructed *solely* based on data from the *nominal* configuration. This greatly reduces the number of flight-hours required to collect enough data to model the aircraft accurately over the entire flight envelope with varying loading configurations. This modeling technique is an attractive choice for a package-delivery vehicle since the stitched model can extrapolate to a loading configuration for an arbitrary payload and provide a model and trim data for analysis and flight control design.

The stitched model's extrapolation is evaluated using off-nominal truth data collected from flight tests of the heavy configuration in the form of both trim controls/states as well as frequency responses. The stitched model is extrapolated at every 1 knot between 0 and 25 knots for both the nominal and heavy configurations. The resulting trim state and control variations for both configurations are shown in Fig. 15. The nominal trim, as expected, matched perfectly while the heavy configuration's trends are well predicted.

The extrapolated models are also compared in the frequency domain with the heavy configuration's flight data that were *not* used to develop the stitched model. Figure 16a shows that the stitched model is able to perfectly capture the distinct trends in both magnitude and phase of the u-body acceleration response at the sensor (flight computer), which is sensitive to center of gravity shifts produced by the specifically designed heavy configuration. Figure 16b shows that the roll rate response's variation is a clear gain offset in the magnitude response due to an increase in I_{xx}. Figure 16 shows that the extrapolated stitched model can very accurately predict the heavy configuration's frequency responses despite *only* being developed from data based on the *nominal* model. The stitched model is only provided with the mass properties of the heavy configuration and it is able to extrapolate from the nominal model and produce a very accurate model of it.
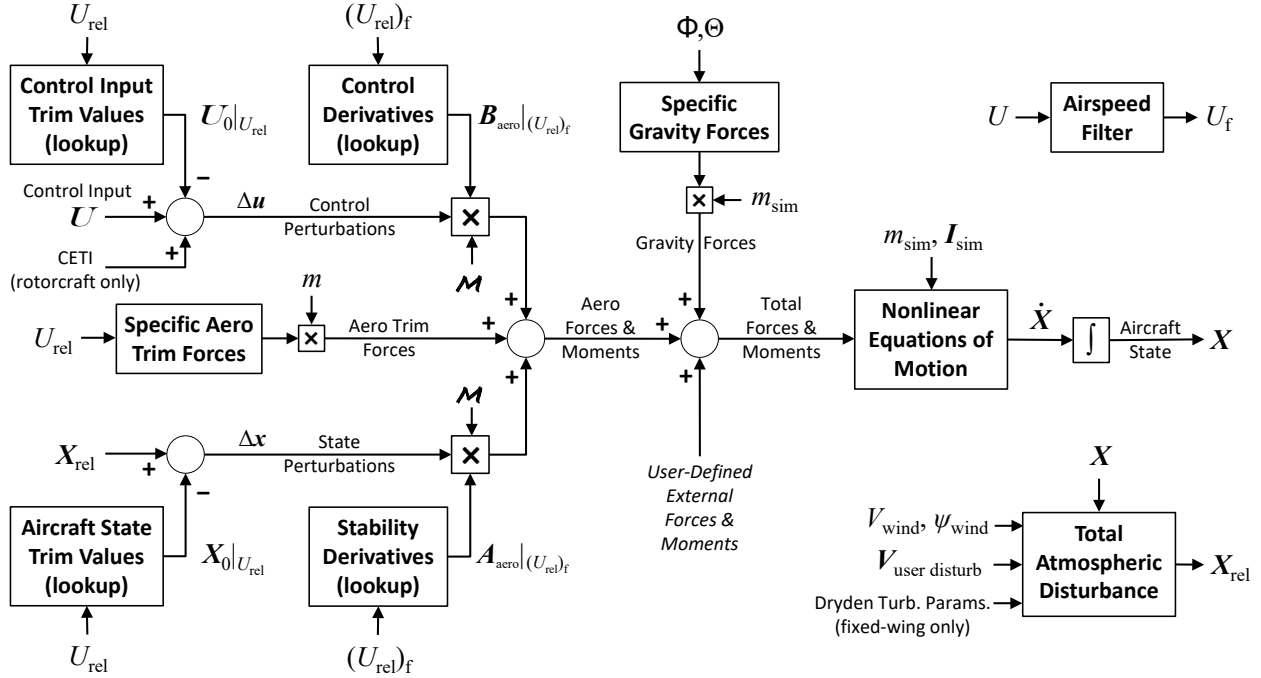
14

Fig. 12   Model stitching architecture [10]

V. Conclusion

Flight tests were conducted on a custom octocopter platform with a large attached cargo bay. Frequency sweeps, doublets, and trim shot data for two, nominal and heavy, loading configurations were flown for system identification and model stitching. State-space models were identified at 0, 10, and 20 knots with average costs of 75.23, 90.66, 61.88, respectively. The models were verified in the time domain using doublets that showed the models properly capture the actual aircraft responses. The three point models were used as anchor points and stitched together with trim shot data to produce a stitched model. The stitched model was validated and showed excellent agreement with the anchor points models. It was also used to extrapolate to the heavy configuration and showed that trim data and predicted responses were accurately predicted when compared to truth flight data. The following conclusions are drawn from the flight testing, identification, and model stitching of this representative package-delivery vehicle.

1) 30-second automated frequency sweeps from 0.628-62.8 rad/sec (0.1-10 Hz) cover a frequency range slow enough to directly identify the speed derivatives and fast enough to capture the actuator's bandwidth for a vehicle
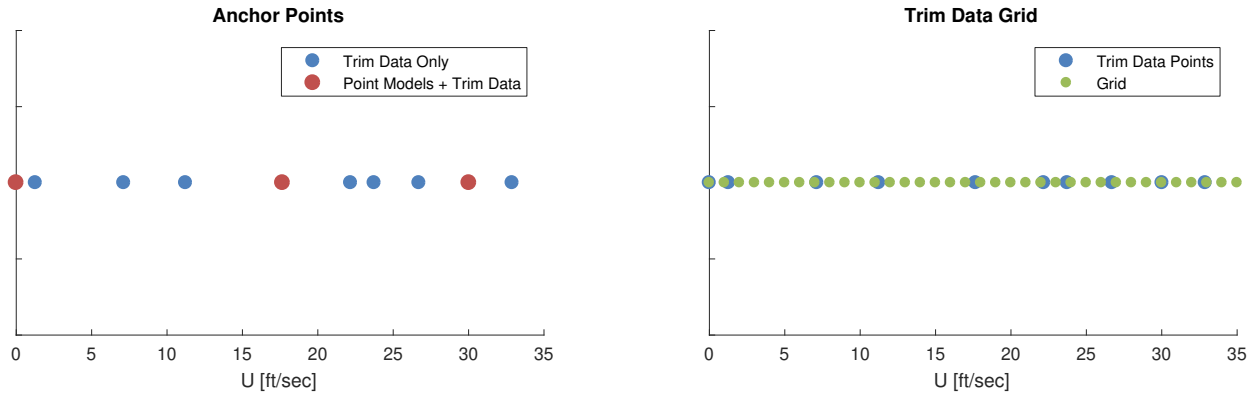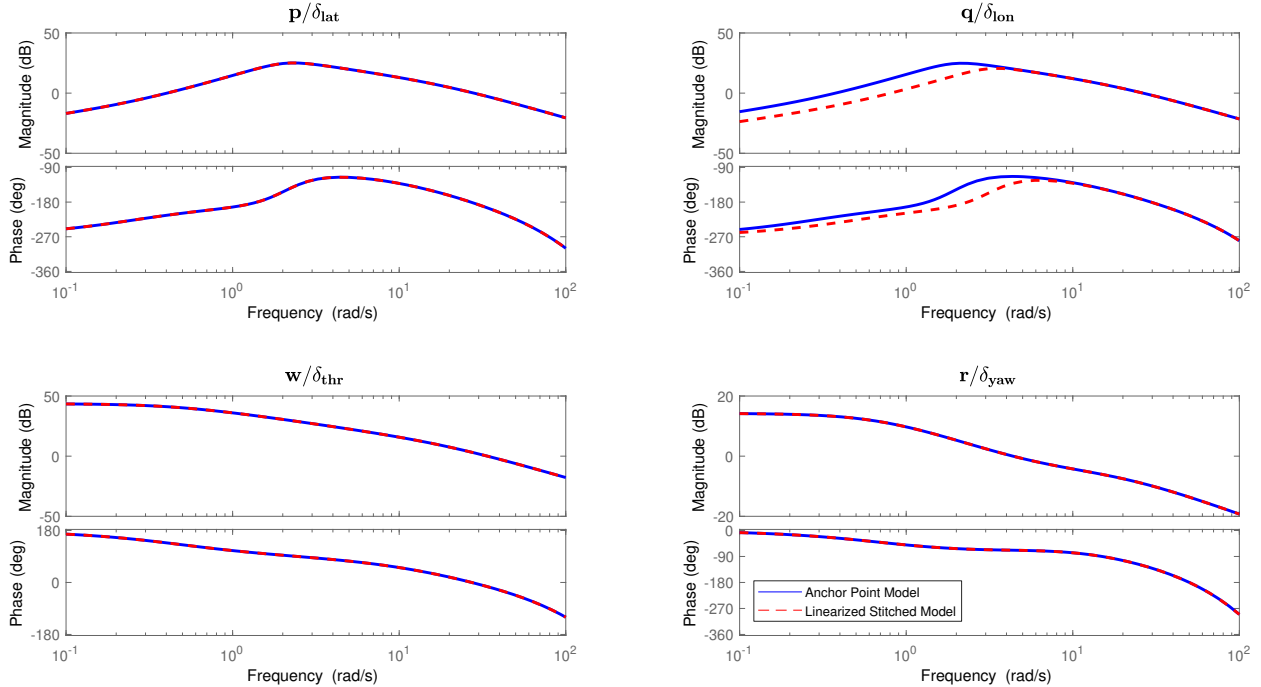

Fig. 13   (a). Overview of the anchor point models and trim data used to construct a stitched model and (b) the rectangular grid of finely spaced trim data.

**Fig. 14 Response comparison between the point models and re-linearized stitched model in hover.**

of this size.

2) The yaw-rate response can be well captured by identifying a zero such that the actuator model has the form of a lead-lag while the responses of the other three axes only require a lag to properly model the actuator.

3) Three anchor point models spaced 10 knots apart and trim shot data collected every 2-3 knots is sufficient for extrapolated models to capture trends in the equilibrium states and controls.

4) The stitched model is able to accurately predict the trim and frequency responses of a heavily corner-loaded configuration carrying 11.7 lb. through extrapolation. This enables models of any arbitrary loading configuration to be produced by the stitched model with confidence since it is anchored by accurate flight-identified point models.

References

[1] Bresciani, T., "Modelling, Identification and Control of a Quadrotor Helicopter," Master's thesis, 2008.

[2] Bangura, M., and Mahony, R. E., "Nonlinear Dynamic Modeling for High Performance Control of a Quadrotor," Australasian Conference on Robotics and Automation, 2012.

[3] Niemiec, R., and Gandhi, F., "Effects of Inflow Modeling on Simulated Aeromechanics of a Quadrotor Helicopter," American Helicopter Society 72nd Annual Forum, 2016.

[4] Zivan, L., and Tischler, M. B., "Development of a Full Envelope Helicopter Simulation Using System Identification," Journal of the American Helicopter Society, 2010, pp. 1–15.

[5] Berger, T., Tischler, M. B., Hagerott, S. G., Cotting, M. C., Gray, W. R., Gresham, J., George, J., Krogh, K., D'Argenio, A., and Howland, J., "Development and Validation of a Flight-Identified Full-Envelope Business Jet Simulation Model Using a Stitching Architecture," AIAA Modeling and Simulation Technologies Conference, 2017.

[6] Knapp, M. E., Berger, T., Tischler, M. B., and Cotting, M. C., "Development of a Full Envelope Flight Identified F-16 Simulation Model," 2018 AIAA Atmospheric Flight Mechanics Conference, 2018.

[7] Tobias, E. L., Sanders, F. C., and Tischler, M. B., "Full-Envelope Stitched Simulation Model of a Quadrotor using STITCH," American Helicopter Society 74th Annual Forum, 2018.
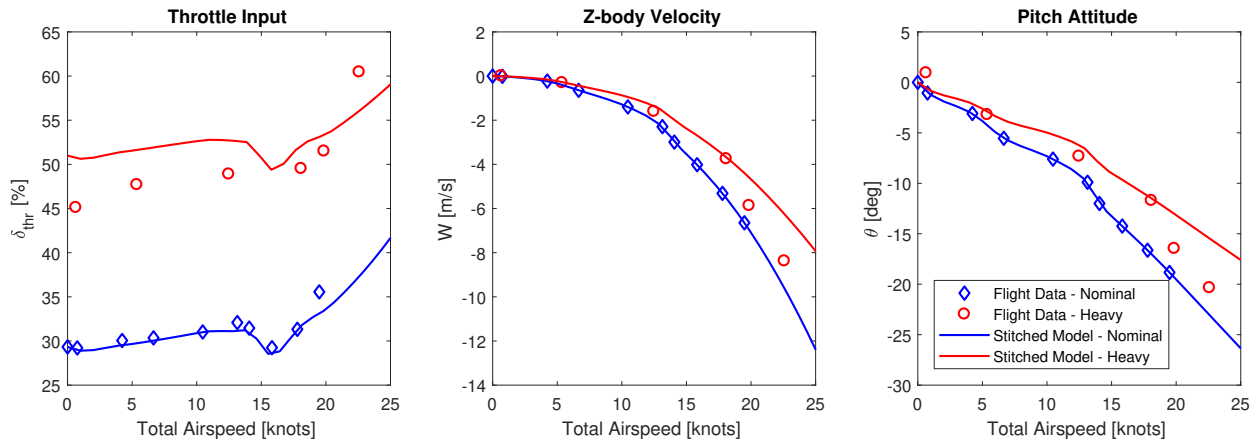
Fig. 15 Comparison of extrapolated trim states and controls with flight data for both nominal and heavy configurations.

[8] Cheung, K. K., Wagster, J. A., Tischler, M. B., Ivler, C. M., Berrios, M. G., Berger, T., Juhasz, O., Tobias, E. L., Goerzen, C. L., Barone, P. S., Sanders, F. C., and Lopez, M. J. S., "An Overview of the U.S. Army Aviation Development Directorate Quadrotor Guidance, Navigation, and Control Project," *American Helicopter Society 73rd Annual Forum*, 2017.

[9] Tischler, M. B., and Remple, R. K., *Aircraft and Rotorcraft System Identification: Engineering Methods and Flight Test Examples Second Edition*, American Institute of Aeronautics and Astronautics, 2012. doi:10.2514/4.861352, URL https://doi.org/10.2514/4.861352.

[10] Tobias, E. L., and Tischler, M. B., "A Model Stitching Architecture for Continuous Full Flight-Envelope Simulation of Fixed-Wing Aircraft and Rotorcraft from Discrete-Point Linear Models," *U.S. Army AMRDEC Special Report RDMR-AF-16-01*, 2016.
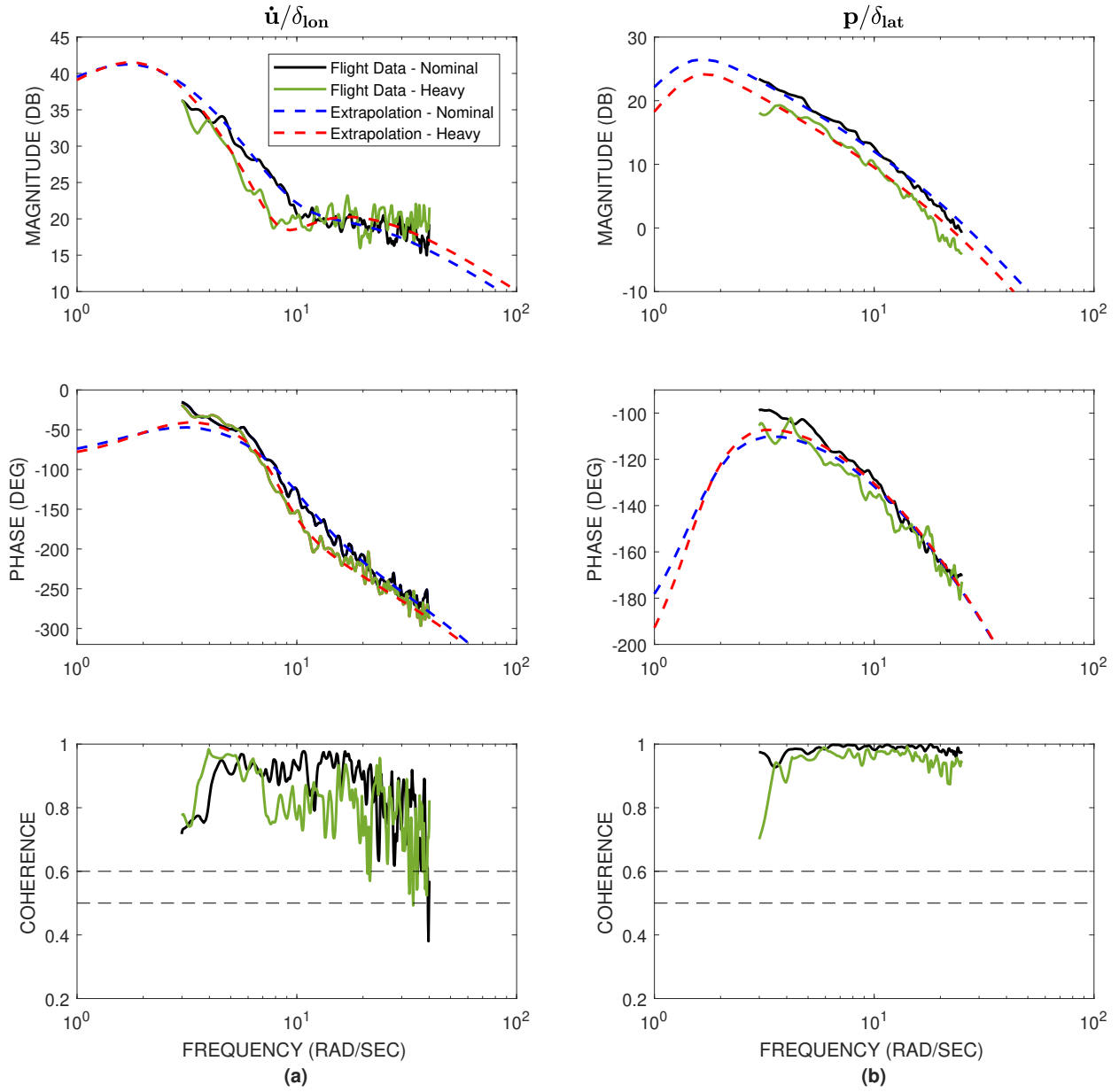
Fig. 16 Frequency response comparisons of (a). $\frac{\dot{u}}{\delta_{lon}}$ **and (b).** $\frac{p}{\delta_{lat}}$ **between the truth flight data and the extrapolated stitched model for both nominal and heavy configurations at 10 knots.**